Mössbauer Effect Reference and Data Journal

May 2017 • Volume 40 • Number 3

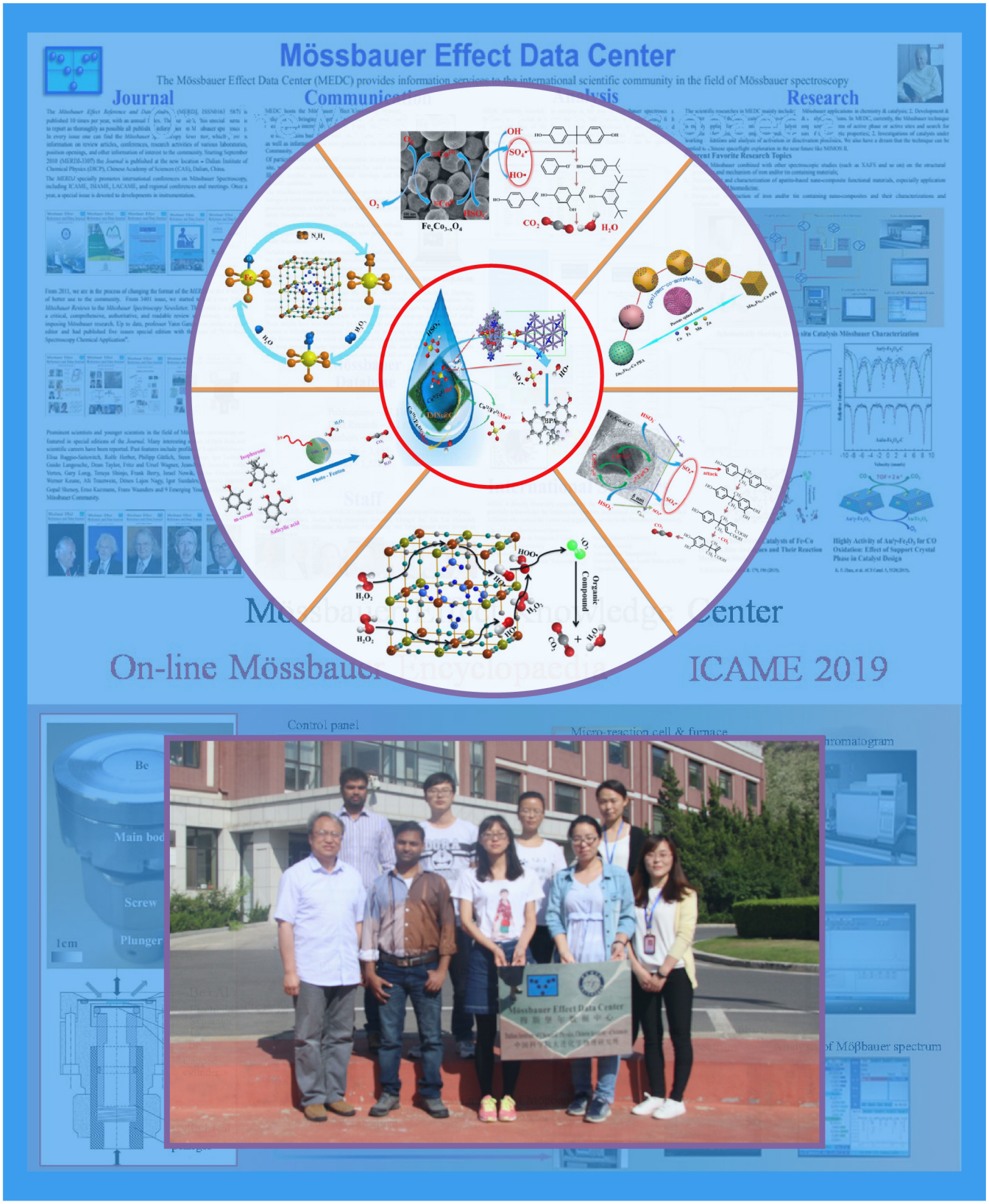

MÖSSBAUER SPECTROSCOPY
NEWSLETTER

May 2017

Mössbauer spectroscopic investigation of Prussian blue analogues and their derivates applied for environmental catalysis and electrochemistry

Xuning Li,[a,b] Junhu Wang [a](✉)
[a]Mössbauer Effect Data Center, Dalian Institute of Chemical Physics, Chinese Academy of Sciences, Dalian 116023, China
[b]University of Chinese Academy of Sciences, Beijing 100049, China
Email: wangjh@dicp.ac.cn

Biography

Xuning Li is currently a PhD doctoral student of Dalian Institute of Chemical Physics, Chinese Academy of Sciences. His research field is related to "Shape-controlled synthesis of MOFs and transition metal-oxide/nitride nanosystems", "Catalytic elimination of environmental pollutants" and "electrocatalysis" etc. He has published 7 high-quality papers on world-renowned journals such as ACS Nano, Nanoscale, Appl. Catal. B, Catal. Sci. Technol. and Catal. Commun. etc. Two of these publications appeared as Top 25 Hottest Articles (July to September 2015) in Science Direct. He has won the "SABIC-CAS scholarship" from Chinese Academy of Sciences, which has only 30 candidates per year in China.

Junhu Wang is a Professor of Chemistry, main research fields are Mössbauer spectroscopic applications and nanometer catalytic materials. He was graduated from Radiochemistry Major, Lanzhou University in 1991. He was awarded the master's and doctor's degrees (jointly trained with Japan Atomic Energy Research Institute) of Toho University (Japan) in 1998 and 2002, respectively. He holds many titles and awards, such as full professor & group leader of Dalian Institute of Chemical Physics (DICP), Chinese Academy of Sciences (CAS), winner of "Hundred Talents Program" honor of introducing outstanding talents from abroad and the financial incentives, Secretary-general of Mössbauer Effect Data Center (MEDC), Executive Editor of Mössbauer Effect Reference and Data Journal (MERDJ), Executive Chairman of 8th International Symposium on the Industrial Applications of the Mössbauer Effect, Member of Councils of China Nuclear Physics Society (CNPS) and Chinese Mössbauer Community. Advisor Member of International Board on the Applications of

the Mössbauer Effect (IBAME), Members of American Chemical Society (ACS) and Chinese Chemical Society (CCS). Over the years, he served at Tokyo National University of Fine Arts and Music (Japan), National Institute for Materials Science (NIMS), National Institute of Advanced Industrial Science and Technology (AIST), and Chukyo University for scientific research and teaching, during which he engaged in researches on Mössbauer spectroscopic studies on structural chemistry of lanthanide and actinide element compounds, hydrogen generation from photocatalytic water splitting over oxide semiconductors, pollutants degradation and mineralization with hydroxyapatite (HAP)/ titania nanocomposited photocatalysts, spectroscopic studies on heterogeneously nanocomposited and cation/anion codoped novel titanium oxide photo-catalytic materials, surface chemistry of phosphate-base catalytic materials, highly active and anti-sinter HAP supported gold catalysts, shape-controlled synthesis of noble metal and composite oxide based electrocatalytic materials, Prussian blue analogues (PBAs) and spinel double oxides developments for removing pollutants in water as well as reactive adsorption materials for fuel-desulfurization and toxic metal ions purification. Current Research Interests: 1) Novel and highly efficient environmental & energy catalytic materials; 2) Novel and highly efficient reactive adsorption materials; and 3) The development and applications of in-situ advanced spectroscopic techniques.

Abstract

Nowadays, the scarcity of fresh water resources and the ever-growing environmental pollution have been attracting increased concern. The Fenton-like process has been widely investigated due to its high efficiency in removing persistent organic contaminants by in-situ production of $SO_4•^-$ or HO• radicals. However, limited mechanism understanding hinders any significant advances in Fenton chemistry. In the past five years, Prof. Junhu Wang's team in the Mössbauer Effect Data Center have made a series of progress in investigating the mechanism of Fenton-like reaction, by using Mössbauer technique determine the coordination environment, spin state and oxidation state of iron ions. Herein, we systematically reviewed the application of Prussian blue analogues (PBAs) in the research fields such as shape-controlled synthesis of multi-metal nitrides (oxides), and their applications in catalytic activation H_2O_2/PMS based Fenton-like reactions for the removal of organic pollutants. Mössbauer technique was applied to investigate the mechanism of the Fenton-like reaction, as well as the structure-function relationship between the catalysts and their activities.

Introduction

Among various advanced oxidation processes (AOPs), Fenton and Fenton-like processes have been widely investigated in view of their high efficiency, simplicity and environmental friendliness [1-3]. Reactive oxygen species (HO•, HO_2• etc.), generated during the Fenton process through **Eq. 1-2**, are highly efficient in degrading nearly all organic compounds rapidly and none selectively [4]. However, because the reaction rate of ferric ions with H_2O_2 (**Eq. 2**) is much slower than that of ferrous ions with H_2O_2 (**Eq. 1**), ferric ions are quickly accumulated during the Fenton reactions. Therefore, a large amount of research focuses on

$$Fe^{2+} + H_2O_2 \rightarrow Fe^{3+} + HO• + OH^- \quad k_1 = 76\ M^{-1}S^{-1} \qquad (1)$$

$$Fe^{3+} + H_2O_2 \rightarrow Fe^{2+} + HO_2• + H^+ \quad k_2 = 0.02\ M^{-1}S^{-1} \qquad (2)$$

accelerating the Fe^{II}/Fe^{III} redox cycle to increase the pseudo first-order rates of the Fenton system [5-17]. Reducing agents (RAs), such as hydroxylamine [8], ascorbic acid [10], quinone [13], humic acid [14] etc., were reported to be effective in accelerating the reduction of Fe^{III} to Fe^{II}, which further enhances the oxidation performance of the Fenton system. However, they may also compete for the active sites of the catalyst with organic compounds and the oxidant (H_2O_2), leading to the decrease of Fenton activity [17-19]. In addition, the limited understanding of the mechanism of heterogeneous Fenton reactions in presence of RAs hinders any significant advances in Fenton chemistry.

In our research, Prussian blue/TiO_2 nanocomposites were first designed to explore the synergistic effects between photocatalyst and Fenton-like system [5]. Then, two kinds of Fe-Co Prussian blue

analogues (Fe-Co PBAs) with different iron valence state, $Fe_3[Co(CN)_6]_2 \cdot 12H_2O$ and $Fe[Co(CN)_6] \cdot 2H_2O$, were developed as novel photo-Fenton catalysts for in-depth investigation of the heterogeneous Fenton reaction mechanism [20]. To further study the reaction intermediates and pathway of active iron species during the Fe-Co PBA catalyzed Fenton-like process, hydrazine (Hz) was newly introduced to enhance the oxidation performance of the Fenton system [21]. Combining the XPS and Mössbauer results, the Hz coordinated iron site (H_2NH_2N-Fe), which is evolved from the original water coordinated iron site (H_2O-Fe), was identified as a more active site which largely increased the reaction rate. Considering that although CN^- is closely associated with stable $[Co(CN)_6]^{3-}$ complex, one may prefer to use oxide in place of cyanide catalysts. $Fe_xCo_{3-x}O_4$ nanocages derived from Fe-Co PBAs were also developed as excellent catalysts for removal of bisphenol A by activation of peroxymonosulfate (PMS) [22]. All through these researches, ^{57}Fe Mössbauer spectroscopy plays a crucial role to determine the oxidation state and the coordination environment of iron species in the catalysts. The octahedral-site Mn^{III}/Mn^{IV} content in $Mn_xFe_{1.8-x}Co_{1.2}O_4$, mainly determined by sensitive ^{57}Fe Mössbauer and XPS techniques, was discovered to be directly correlated with the oxygen reduction/evolution reaction (ORR/OER) activity [23].

In addition, series of bimetallic Fe_xCo_y@C nanocages were newly synthesized via a one-step thermal decomposition of Fe_yCo_{1-y}-Co PBAs nanospheres in nitrogen atmosphere at different temperatures and developed as Fenton-like catalysts to activation PMS for BPA removal [24]. A novel strategy based on a one-step thermal decomposition of MOFs in N_2 atmosphere was developed for shape-controlled synthesis of graphene encapsulated transition metal nitrides (TMNs) ($Fe_xMn_{6-x}Co_4$-N@C). The catalytic oxidation performance of the as-synthesized $Fe_xMn_{6-x}Co_4$-N@C nano-dices in BPA degradation by PMS activation was found largely enhanced with the increasing of the content of Mn_4N [25].

1. Prussian blue/TiO_2 nanocomposites as a heterogeneous photo-Fenton catalyst for degradation of organic pollutants in water

1.1. Synthesis of Prussian blue/TiO_2 nanocomposites (PB/TiO_2 NPs)

PB/TiO_2 NPs with different loading of PB were synthesized by a simple chemical solution deposition method [26]. Briefly, a ferrocyanide solution (0.03 M) and a TiO_2 solid powder at different stoichiometric molar ratios of PB and TiO_2 were dissolved in 15 mL water, followed by magnetically stirring for 30 min at ambient temperature. In the mixed colloid solution, 15 mL ferric chloride solution (0.04 M) was added slowly with continuous stirring for another 30 min. The colloid solution was aged for at least 12 hours, which resulted in precipitates. Finally, the precipitate was centrifuged and washed with deionized water three times and the resulting product was dried in an oven at 333 K for 12 hours. One ^{57}Fe enriched PB ($^{57}Fe^{III}_4[Fe^{II}(CN)_6]_3$)/$TiO_2$ sample with a molar ratio of 1/60 was prepared by the same method as that used to synthesize the other samples but instead of $FeCl_3$ solution by using $^{57}FeCl_3$ stock solution for Mössbauer characterization.

1.2. Reaction mechanism and reactive intermediates

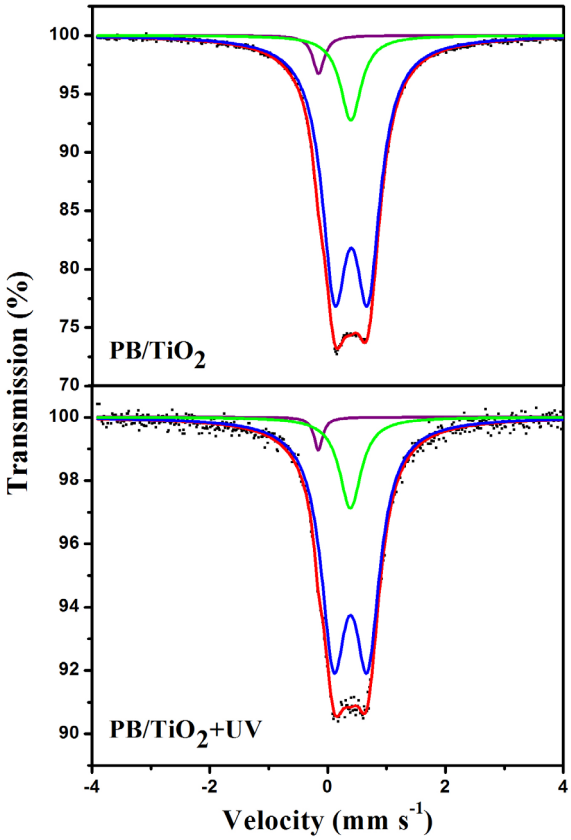

Fig. 1. Room temperature ^{57}Fe Mössbauer spectra of PB($^{57}Fe^{III}_4[Fe^{II}(CN)_6]_3$)/$TiO_2$ with and without UV irradiation. The green and blue solid lines represent the high-spin Fe^{III} component in PB with different coordination environment, respectively. The purple solid line represents the low-spin Fe^{II} component in PB.

Initially, attempt was made to examine if any change in valence of iron via electron-transfer in the studied heterogeneous system occurred. The ^{57}Fe Mössbauer spectroscopy is an ideal method for determining the oxidation state and spin-state of iron ions in a solid. The parameters of the Mössbauer spectroscopy, isomer shift (IS) and quadruple splitting (QS) are listed in **Tables 1 and 2**. IS is sensitive to the iron valence state while QS varies with the coordination environment. **Fig. 1** shows the Mössbauer spectra of ^{57}Fe enriched $PB(^{57}Fe^{III}_4[Fe^{II}(CN)_6]_3)/TiO_2$ NPs sample with and without UV irradiation. The ^{57}Fe enrichment into the high-spin site Fe^{III} allowed us to confirm that the UV irradiation had no effect on the values of the hyperfine parameters of this site. This suggests that high-spin Fe^{III} in PB/TiO_2 NPs could not be reduced to high-spin Fe^{II} by photo-induced electrons of TiO_2. It could be that the electron-transfer in PB/TiO_2 in photo-Fenton process only occurred on the low-spin Fe^{II}.

Table 1. Room temperature ^{57}Fe Mössbauer parameters of different simulated systems obtained by Model I

System	Component	IS (mm s^{-1})	QS (mm s^{-1})	Area (%)
PB/TiO_2	LS Fe^{II}	-0.152		19
	LS Fe^{III}	-0.143	0.144	16
	HS Fe^{III}	0.393	0.583	65
$PB/TiO_2+H_2O_2$	LS Fe^{II}	-0.152		15
	LS Fe^{III}	-0.147	0.144	20
	HS Fe^{III}	0.387	0.595	65
$PB/TiO_2+H_2O_2+UV$	LS Fe^{II}	-0.154		19
	LS Fe^{III}	-0.149	0.144	15
	HS Fe^{III}	0.383	0.606	66

Experimental errors are ± 0.001 mm s^{-1} for isomer shift (IS), ± 0.005 mm s^{-1} for quadrupole splitting (QS) and 1% for relative area. IS is relative to α-iron foil.

Table 2. Room temperature ^{57}Fe Mössbauer parameters of different simulated systems by Model II

System	Component	IS (mm s^{-1})	QS (mm s^{-1})	Area (%)
PB/TiO_2	LS $Fe^{II/III}$	-0.152		35
	HS Fe^{III}	0.384	0.602	65
$PB/TiO_2+H_2O_2$	LS $Fe^{II/III}$	-0.142		35
	HS Fe^{III}	0.389	0.565	65
$PB/TiO_2+H_2O_2+UV$	LS $Fe^{II/III}$	-0.153		34
	HS Fe^{III}	0.377	0.621	66
(^{57}Fe) PB/TiO_2	LS Fe^{II}	0.363		16
	HS Fe^{III}	0.373	0.59	84
(^{57}Fe) PB/TiO_2+UV	LS Fe^{II}	0.362		17
	HS Fe^{III}	0.366	0.598	83

Experimental errors are ± 0.001 mm s^{-1} for isomer shift (IS), ± 0.005 mm s^{-1} for quadrupole splitting (QS) and 1% for relative area. IS is relative to α-iron foil.

The electron-transfer in PB/TiO_2 in photo-Fenton process was investigated by carrying out a series of Mössbauer measurements focusing on the low-spin site in non-enriched samples. The low-spin Fe^{II} and Fe^{III} are difficult to distinguish in bulk Prussian blue particles [27], but for the nanoparticles, it was easier because of the large specific surface area and thus more electron-transfer reactions could be happened. Considering that the electron-transfer rate (τ_r) related to Fenton reaction cycle might be in two different regimes with respect to the characteristic time in Mössbauer spectroscopy ($\tau_M \approx 10^{-8}$ s) [28], the Mössbauer spectra were analyzed using two models, which are described below.

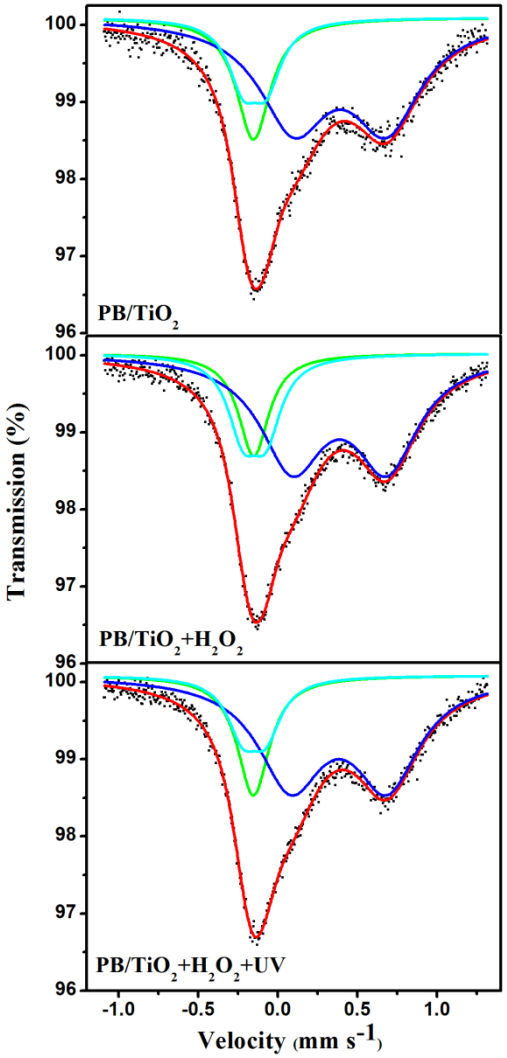

Fig. 2. Room temperature ^{57}Fe Mössbauer spectra of PB/TiO_2 NPs with a molar ratio of 1/60 at different systems. The green singlet and blue doublet subspectra represent the low-spin Fe^{II} and high-spin Fe^{III} components, and the cyan doublet represents the low-spin Fe^{III} component.

Model I: slow electron-transfer between low-spin Fe^{II} and Fe^{III}. This model is applicable when the electron-transfer is slower than the characteristic time of Mössbauer spectroscopy. Because the low-spin Fe^{III} has five electrons in the t_{2g} orbital group, it should have some quadruple splitting [29]. The finite value of QS originates from the valence electron term if the electron-transfer on the surface of nanoparticle is slower than 10^{-8} s. The spectra with a quadrupole doublet for low-spin Fe^{III} and a singlet for low-spin Fe^{II} are shown in **Fig. 2**. From this model, we could identify the percentages of low-spin Fe^{III} and Fe^{II} in different reaction conditions. The increase of low-spin Fe^{III} was observed when the reaction with H_2O_2 was conducted, however, after the irradiation by UV lamp, the percentage of low-spin Fe^{III} changed back to its original value as listed in **Table 1**. This supports the reduction of low-spin Fe^{III} by the photo-induced electrons of TiO_2.

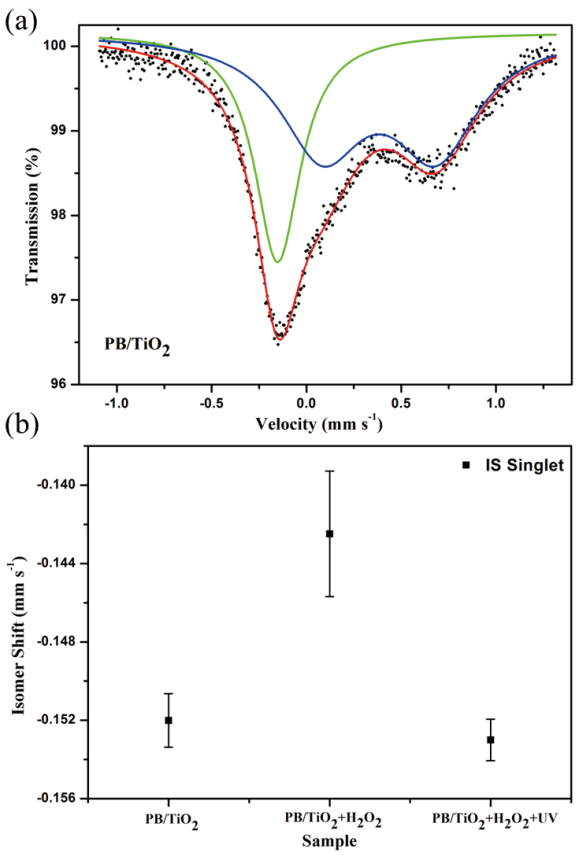

Fig. 3. (a) Room temperature Mössbauer spectrum of PB/TiO_2 with a molar ratio of 1/60. The singlet and doublet subspectra represent the low-spin Fe^{II} and high-spin Fe^{III} components, respectively, and (b) the isomer shifts of low-spin Fe^{II} measured at different systems

Model II: fast electron-transfer between low-spin Fe^{II} and Fe^{III}. This model is applicable when the electron-transfer is faster than the characteristic time of Mössbauer spectroscopy. The spectra using the model of an average valence was analyzed. In this model, as the electron-transfer was very fast, we describe the state of low-spin iron (average between Fe^{II} and Fe^{III}) by a singlet subspectrum as shown in **Fig. 3**. Since the crystallographic environments of the low-spin Fe^{II} and Fe^{III} were very similar, the time averaging of the electron density would result in some intermediate value of the isomer shift. The isomer shift of the low-spin mixed-valent state Fe^{II}/Fe^{III} changed from -0.152 mm s^{-1} to -0.142 mm s^{-1} when we conducted the in-situ reaction with H_2O_2 (**Table 2**). This may be due to shift of the electron density towards more oxidized state (Fe^{III}) [30]. After the irradiation by UV lamp, the IS changed to its original value of -0.153 mm s^{-1}. This indicates the shift of the average valence state towards more reduced state (Fe^{II}) owing to the participation of the photo-induced electrons of TiO_2, also supports the reduction of low-spin Fe^{III} by the photo-induced electrons of TiO_2.

1.3. Synergistic effect of PB/TiO_2 NPs as a heterogeneous photo-Fenton catalyst

In order to evaluate the synergistic effects between photocatalysis and Fenton reactions, PB/TiO_2 NPs with different loading of PB were synthesized and a series of RhB degradation experiments was carried out for comparison. **Fig. 4** shows the first-order rate constants of PB/TiO_2 NPs with different molar ratios under different reaction systems. There was no activity of PB/TiO_2 NPs with different molar ratios under UV irradiation without H_2O_2. The reason should be the same as that mentioned above for the PB/TiO_2 NPs with a molar ratio of 1/60. This supports the synergism between the TiO_2 photocatalysis in the photo-Fenton process. With the assistance of UV and H_2O_2, the photo-induced electrons of TiO_2 could reduce the Fe^{III} in PB oxidized by H_2O_2, thus increasing the reaction rate.

The Fenton activity of PB/TiO_2-H_2O_2 increased linearly with the increase of PB loading on the surface of TiO_2. This is because PB ($Fe^{III}{}_4[Fe^{II}(CN)_6]_3$) contained Fe^{II}, the activity increased with the increase of iron. However, when the mole ratio of

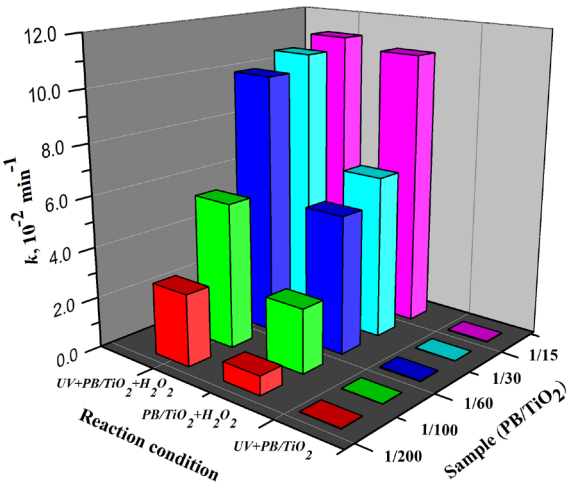

Fig. 4. The rate constants of the RhB degradation over PB/TiO_2 NPs with different molar ratios in different systems. Reaction conditions: [RhB] = 12 mg L^{-1}, [H_2O_2] = 0.4 M (if needed), catalyst = 1.0 g L^{-1} (if needed), T = 308 K, and 27 W black light with 2.5 mW cm^{-2} intensity (if needed).

PB/TiO_2 was 1/15, UV light seemed to have no more contribution to the photo-Fenton reaction. This may be explained by considering that high surface coverage of TiO_2 by PB NPs could inhibit penetration of UV light to the surface of TiO_2. In subsequent experiments, the mole ratio of PB/TiO_2 = 1/60 was chosen because it yielded the maximum synergism in the photo-Fenton process.

The steps of oxidation of organic pollutants in water by the photo-Fenton process are described by reactions 5-9. Without the UV irradiation, the reaction between PB and H_2O_2 generates •OH and the Fe^{III} containing species in PB (reaction 3). However, Fe^{III} is further reduced by H_2O_2 to Fe^{II} (reaction 4). This later step regenerates PB for further utilization in the Fenton reaction. In the presence of UV radiation in the PB/TiO_2-H_2O_2 system, reactions 7-9 also occur, leading to enhanced degradation. UV irradiation of the surface of TiO_2 induces electron and hole pairs (reaction 5). The hole oxidizes the water molecule to produce •OH. Therefore •OH is produced from two reactions (3 and 6) in the photo-Fenton system which results in the increased removal efficiency of RhB compared to that obtained in dark Fenton process. Moreover, the electron induced in reaction 5 can reduce Fe^{III} species in [Fe^{III}–$(NC)_6$–Fe^{III}] to give

back PB (reaction 7). Hence, regeneration of PB is possible from two reactions 4 and 7, which facilitate the Fenton reaction in the studied system. **Reactions 3-7** support the postulated mechanism.

$$[Fe^{III}–(NC)_6–Fe^{II}] + H_2O_2 \rightarrow [Fe^{III}–(NC)_6–Fe^{III}] + \bullet OH + OH^- \quad (3)$$

$$[Fe_{III}–(NC)_6–Fe^{III}] + H_2O_2 \rightarrow [Fe^{III}–(NC)_6–Fe^{II}] + H_2O + 1/2O_2 \quad (4)$$

$$TiO_2 + h\nu \rightarrow e^- + h^+ \quad (5)$$

$$h^+ + H_2O \rightarrow \bullet OH + H^+ \quad (6)$$

$$[Fe^{III}–(NC)_6–Fe^{III}] + e^- \rightarrow [Fe^{III}–(NC)_6–Fe^{II}] \quad (7)$$

2. Excellent Photo-Fenton Catalysts of Fe-Co PBAs and Their Reaction Mechanism Study

2.1. Synthesis of Fe-Co PBAs

$Fe_3[Co(CN)_6]_2•12H_2O$ (Fe^{II}-Co PBA) and $Fe[Co(CN)_6]•2H_2O$ (Fe^{III}-Co PBA) were prepared by reaction of aqueous solutions of $FeCl_2•4H_2O$ or $FeCl_3•6H_2O$ and $K_3[Co(CN)_6]$. The preparation process was similar to previous reports [21, 26] but with slight modification. Typically, 25 mL $K_3[Co(CN)_6]$ aqueous solution (0.10 M) was slowly added into 25 mL $FeCl_2•4H_2O$ or $FeCl_3•6H_2O$ aqueous solution (0.10 M) under magnetic stirring. The mixed solution was further stirred for another 30 min and aged for 1 day. Finally, the resulting precipitates were centrifuged and washed for at least three times with deionized water, followed by drying in an oven at 333 K for 12 hours. For comparison, the insoluble PB sample was synthesized by the same process as that of Fe^{III}-Co PBA, except the replacement of $K_3[Co(CN)_6]$ (0.10 M) using $K_4[Fe(CN)_6]•3H_2O$ (0.15 M).

2.2. Characterizations of catalysts by Mössbauer spectroscopy and plausible mechanisms of the photo-Fenton reaction over Fe-Co PBAs catalysts

In order to investigate the iron redox cycling and the mechanisms of the photo-Fenton processes over Fe-Co PBA catalysts, ^{57}Fe Mössbauer spectroscopy was applied to determine the oxidation state and coordination environment of iron ions in Fe-Co PBAs under different Fenton reaction conditions (**Fig. 5**). The fitting model of the spectra was same as a previous work to a similar PBA complex [31]. The obtained Mössbauer isomer shifts of Fe^{II}-Co PBA (**Fig. 5a**) suggest that 89% of the Fe species are in high-spin Fe^{II}. In this porous structure with rich of water coordinated Fe (Fe-water), majority of the Fe^{II}/Fe^{III} species are octahedrally coordinated by nitrogen as well as oxygen of water molecules [32]. According to their quadruple splitting values, the irons are ascribed in different chemical environments [29, 33]: 26% of Fe^{II} in octahedral trans-$(H_2O)_2FeN_4$ and $(H_2O)FeN_5$, 32% of Fe^{II} in $(H_2O)_3FeN_3$ with H_2O in facial conformation, and 31% Fe^{II} in cis-$(H_2O)_2FeN_4$ and $(H_2O)_3FeN_3$ in meridional conformation.

Mössbauer spectrum of Fe^{II}-Co PBA after the photo-Fenton reaction (**Fig. 5c**) gives clear evidence that the major part iron ions (92%) was oxidized and the new Fe-O phase was generated during the photo-Fenton process. It is frequently found in Fenton reactions that the oxidation of ferrous species is usually in a higher rate than the inverse process [31, 34]. Indeed, Fe^{III}-Co PBA with Fe^{III} in octahedrally coordinated structure showed considerable photo-Fenton activity even though it is lower than Fe^{II}-Co PBA. The contents of Fe^{II} in Fe^{III}-Co PBA before and after the reaction were both around 4%. No obvious difference between the Mössbauer spectra of Fe^{III}-Co PBA before and after the photo-Fenton reaction also suggests that it is quite stable (**Fig. 5d**). These Mössbauer results made it clear that the iron redox cycling in Fe-Co PBAs occurs during the Fenton processes. The Fe^{II} in Fe-Co PBAs tended to be oxidized by H_2O_2 to produce a new Fe-O phase on the surface of the Fe^{II}-Co PBA nanoparticles. The Fe^{III} could also be reduced by H_2O_2 at a slower rate until the ratio of Fe^{II} and Fe^{III} active sites reached to a certain value. Abundant vacancies and water coordinated iron sites for creating maximal active sites are responsible for the excellent photo-Fenton activities of Fe-Co PBAs.

Generally speaking, at least one coordination position of Fe^{II}/Fe^{III} sites should be opened or occupied by a labile

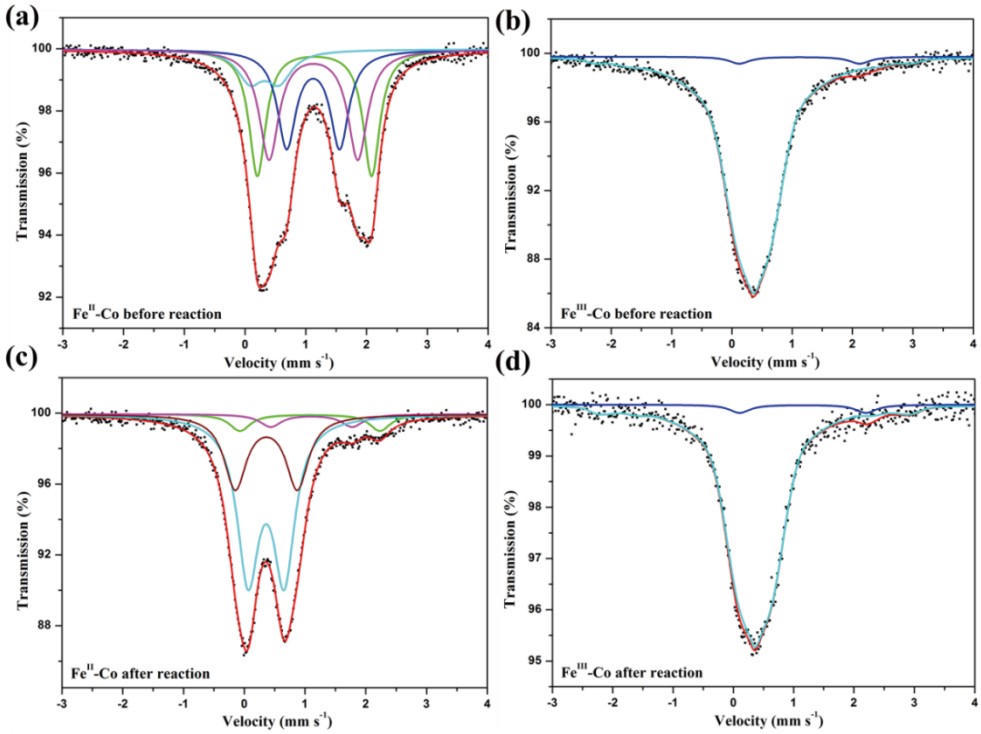

Fig. 5. Room temperature ^{57}Fe Mössbauer spectra of Fe^{II}-Co PBA (a) before, (c) after; Fe^{III}-Co PBA (b) before, and (d) after photo-Fenton reactions. The spectrum of (a) was fitted with four quadrupole doublets. Prevailing external (green color) doublet was assigned to Fe^{II} in octahedral trans-$(H_2O)_2FeN_4$ and trans-$(H_2O)FeN_5$ (1/2trans(H_2O) & 5/4N). Middle doublet (magenta color) was assigned to Fe^{II} in $(H_2O)_3FeN_3$ with H_2O in 3D conformation (3fac(H_2O) & 3N). Inner doublet (blue color) was assigned to cis-$(H_2O)_2FeN_4$ and $(H_2O)_3FeN_3$ with three H_2O in one plane (2cis/3mer(H_2O) & 4/3N). The minor doublet (cyan color) represented to the small amount of high-spin Fe^{III} ions in the Fe^{II}-Co PBA. The spectrum of (c) was fitted in the same model as (a) except for the doublet (purple color) assigned to the newly formed Fe-O species after photo-Fenton reaction. The spectra of (b) and (d) were fitted with two quadrupole doublets. The cyan and blue solid lines represent the high-spin Fe^{III} and Fe^{II} components in Fe^{III}-Co PBA, respectively.

ligand (such as H_2O) for a homogeneous Fenton reaction to occur [35, 36]. The unsaturated or labile ligand coordinated Fe^{II}/Fe^{III} is considered to preferentially form the Fe–peroxide complexes and then produce the hydroxide radicals [37]. Thus, the plausible mechanisms of photo-Fenton reaction over Fe-Co PBAs can be proposed as follows. Taking the iron ion in $(H_2O)FeN_5$ as an example, in the first stage of the Fenton process, the water molecules coordinated to iron sites are replaced by H_2O_2 and form Fe^{II}-peroxide complexes to produce the HO• radicals (**Eq. 8**). However, the oxidation of the majority of iron ions (92%) in Fe^{II}-Co PBA should result in releasing some iron ions to form the new Fe-O phase on the surface of Fe^{II}-Co PBA nanoparticles. The Fe^{III} in Fe-Co PBAs could also be reduced by H_2O_2 at a slower rate to produce superoxide radical (HOO•) through the formation of Fe^{III}-peroxide complexes (**Eq. 9**). In the Fe^{II}-Co PBA, the rate of the reaction expressed by **Eq. 9** is not negligible, therefore, the residual Fe^{II} could be always observed by Mössbauer spectroscopy. In the Fe^{III}-Co PBA, the rates of the reactions expressed by **Eq. 8** and **Eq. 9** should be inversely proportional to the contents of the active sites of Fe^{II} and Fe^{III}, therefore, no change could be observed by Mössbauer spectra.

$$[Fe(CN)_5(H_2O)]^{3-} + H_2O_2 \rightarrow [Fe(CN)_5(HO)_2]^{3-} + H_2O \rightarrow [Fe(CN)_5(H_2O)]^{2-} + HO\bullet + OH^- \quad (8)$$

$$[Fe(CN)_5(H2O)]^{2-} + H_2O_2 \rightarrow [Fe(CN)_5(HO)_2]^{2-} + H_2O \rightarrow [Fe(CN)_5(H2O)]^{3-} + HOO\bullet + H^+ \quad (9)$$

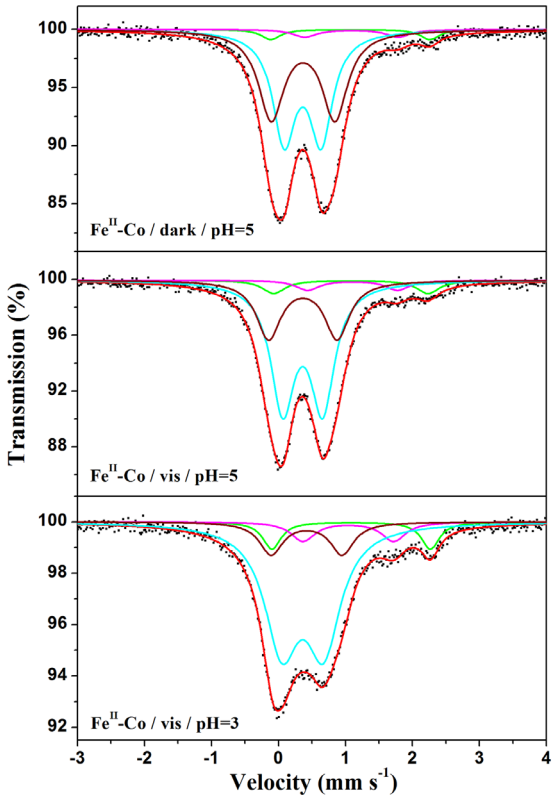

Fig. 6. Room temperature ^{57}Fe Mössbauer spectra of Fe^{II}-Co PBA after the different Fenton reaction condition. The spectra were fitted with four quadrupole doublets. The green color doublet is assigned to Fe^{II} in octahedral trans-$(H_2O)_2FeN_4$ and trans-$(H_2O)FeN_5$ (1/2trans(H_2O) & 5/4N). The magenta color doublet is assigned to Fe^{II} in $(H_2O)_3FeN_3$ with H_2O in 3D conformation (3fac(H_2O) & 3N). The cyan color doublet represents to the high-spin Fe^{III} component in the Fe^{II}-Co PBA. The purple color doublet is assigned to the newly appeared Fe-O species after the photo-Fenton reaction.

The content of Fe^{II} in the Fe^{II}-Co PBA after the photo-Fenton process at pH = 4.8 is 11%, higher than that after the dark Fenton reaction (8%), and smaller than that after the photo-Fenton process at pH = 3.0 (17%). The corresponding Mössbauer spectra are shown in **Fig. 6**. These results indicate that the enhanced Fenton activity with the assistance of either visible light or low pH is caused by the accelerated reduction of Fe^{III} to Fe^{II}. The most probable reason for this acceleration is that the dyes such as RhB could be excited by visible light irradiation, then it could transfer electron to Fe^{III} (**Eqs. 10, 11**) [3, 38].

$$RhB + hv \rightarrow RhB^{*} \quad (10)$$

$$RhB^{*} + Fe^{III} \rightarrow Fe^{II} + RhB^{*+} \quad (11)$$

3. Hydrazine drastically promoted Fenton oxidation of bisphenol A catalyzed by Fe^{III}-Co Prussian blue analogue

3.1. Plausible mechanisms of the Hz promoted Fe^{III}-Co PBA Fenton process

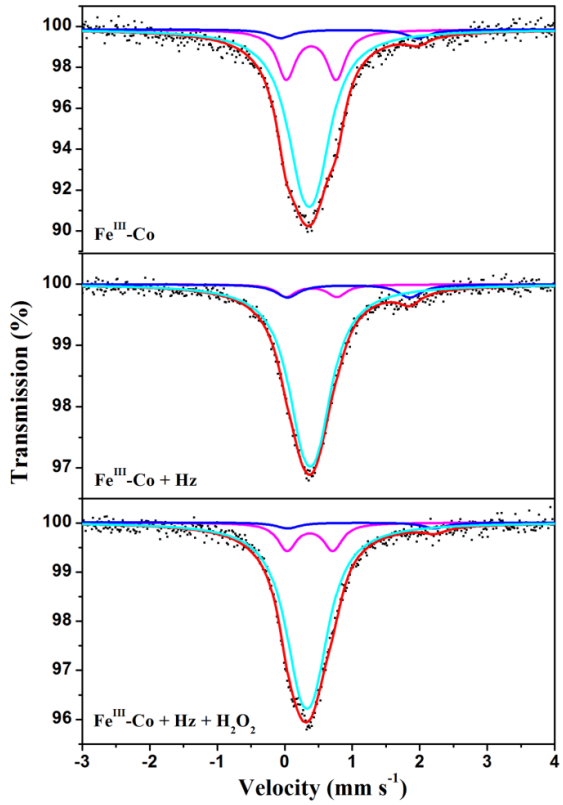

Fig. 7. Room temperature ^{57}Fe Mössbauer spectra of Fe^{III}-Co PBA before and after different reaction system. The spectra of were fitted with three quadrupole doublets. The cyan and magenta doublets are assigned to Fe^{III} in FeN_6 and (H_2O) FeN_5, respectively. The blue doublet is assigned Fe^{II} coordinated with x(H_2O)&(6-x)N in Fe^{III}-Co PBA.

To understand the mechanisms of the Hz promoted Fe^{III}-Co PBA Fenton reaction, it is important to identify the reaction intermediates and pathway of iron species. ^{57}Fe Mössbauer spectroscopy is an ideal technique for determining the coordination environment and oxidation state of iron ions in a solid [5, 20, 22]. The Mössbauer spectra of Fe^{III}-Co PBA before and after different reaction system were measured to explore the changes of the coordination environments of active iron species during the Fenton process. The model of fitting the spectra was similar as in our previous works [20, 39]. As shown in **Fig. 7**, the cyan and magenta doublets could be assigned to six nitrogen coordinated Fe^{III} in $[Fe(CN)_6]^{3-}$

or $[Fe(CN)_5(Hz)]^{2-}$ (defined as: FeN_6) and five nitrogen and one water coordinated Fe^{III} in $[Fe(CN)_5(H_2O)]^{2-}$ (defined as: $(H_2O)FeN_5$), respectively. The blue doublet could be assigned to Fe^{II} existed in Fe^{III}-Co PBA. The content of Fe^{II} in Fe^{III}-Co PBA increased from 4.5% to 7.7% after the reaction with Hz, suggesting that Hz is capable to reduce a part of Fe^{III} to Fe^{II}. More interesting phenomenon is that, the content of Fe^{III} in FeN_6 was increased from 75.0% to 86.5% with the decrease of Fe^{III} in $(H_2O)FeN_5$ from 20.5% to 5.8%. This result indicates that the water coordinated iron site (H_2O-Fe) was partly replaced by Hz coordinated iron site (H_2NH_2N-Fe) during the Hz promoted Fenton process. However, when Hz and H_2O_2 were coexisting in the reaction system, it was of great importance to find that the content of Fe^{III} in $(H_2O)FeN_5$ was higher than the one without H_2O_2. All these results suggest that the reaction of H_2O_2 with $[Fe(CN)_5(Hz)]^{2-}$ is most likely to occur during the Fenton process.

Therefore, considering the Mössbauer results, the water coordinated iron site (H_2O-Fe) could be further identified as the main active site in the Fe-Co PBAs Fenton process. However, in the Hz/Fe^{III}-Co PBA Fenton system, the plausible reaction intermediates and pathway of active iron species could be proposed as follows (**Eqs. 12-16**). Firstly, the Hz could reaction with $[Fe(CN)_5(H_2O)]^{2-}$, replaced the water and produced Hz coordinated iron site, thus increasing the content of Fe^{III} in FeN_6 (**Eq. 12**). Secondly, $[Fe(CN)_5(Hz)]^{2-}$ served as a more active site and reaction with H_2O_2, which produced the HO• radicals. Thirdly, the as-produced Fe^{II} in $[Fe(CN)_5(H_2O)]^{3-}$ could be easily oxidized by H_2O_2 to $[Fe(CN)_5(H_2O)]^{2-}$, with the generation of hydroperoxyl radicals (HOO•). The whole reaction mechanism during the Hz/Fe^{III}-Co PBA Fenton process was shown in **Fig. 8**. All these results clearly demonstrate that the Hz coordinated iron site is most probably the main activity site for the Hz promoted Fe^{III}-Co PBA Fenton process.

$$[Fe(CN)_5(H_2O)]^{2-} + Hz \rightarrow [Fe(CN)_5(Hz)]^{2-} + H_2O \quad (12)$$

$$[Fe(CN)_5(Hz)]^{2-} + H_2O_2 \rightarrow [Fe(CN)_5(H_2O_2)]^{2-} + Hz \quad (13)$$

$$[Fe(CN)_5(H_2O_2)]^{2-} \rightarrow [Fe(CN)_5(H_2O)]^{3-} + HOO\bullet + H^+ \quad (14)$$

$$[Fe(CN)_5(H_2O)]^{3-} + H_2O_2 \rightarrow [Fe(CN)_5(H_2O_2)]^{3-} + H_2O \quad (15)$$

$$[Fe(CN)_5(H_2O_2)]^{3-} \rightarrow [Fe(CN)_5(H_2O)]^{2-} + HO\bullet + OH^- \quad (16)$$

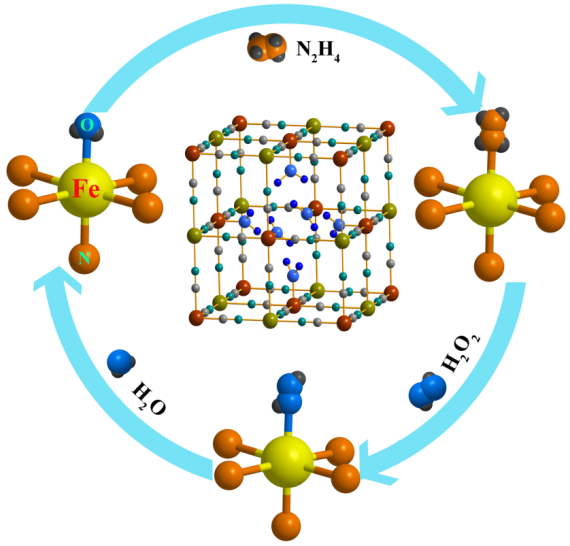

Fig. 8. The plausible reaction intermediates and pathway of active iron species during the Hz/Fe^{III}-Co PBA Fenton process.

4. $Fe_xCo_{3-x}O_4$ nanocages derived from nanoscale metal–organic frameworks for removal of bisphenol A by activation of peroxymonosulfate

4.1. Preparation of $Fe_xCo_{3-x}O_4$ nanocages

Fe_yCo_{1-y}-Co PBAs nanospheres were prepared by the reaction of FeC_{l2}•$4H_2O$ and $CoCl_2$•$6H_2O$ mixture with $K_3[Co(CN)_6]$ in PVP aqueous solution. Typically, desired amounts of FeC_{l2}•$4H_2O$ and CoC_{l2}•$6H_2O$ (totally 9 mM) were dissolved in 40 mL deionized water with PVP (1.2 g) under vigorous stirring. Then 40 mL $K_3[Co(CN)_6]$ aqueous solution (5 mM) was slowly added into the premixed solution. The obtained colloid solution was further stirred for another 30 min and aged for 20 h. The resulting precipitates were centrifuged and washed for at least three times with the mixture of ethanol and deionized water,

followed by drying in an oven at 333 K for 20 h. To obtain the $Fe_xCo_{3-x}O_4$ ($0 < x < 1.0$) nanocages, Fe_yCo_{1-y}-Co PBAs nanospheres were heated at 773 K and kept for 1 h.

4.2. Activation mechanism of PMS over $Fe_{0.8}Co_{2.2}O_4$ nanocages

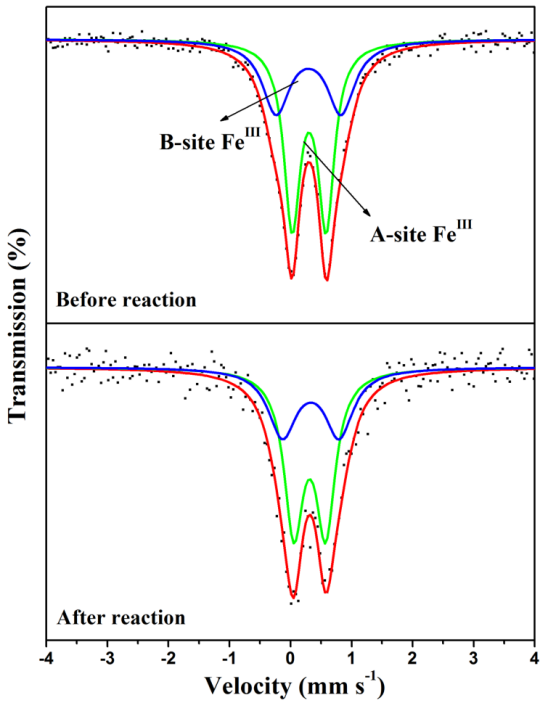

Fig. 9. Room temperature ^{57}Fe Mössbauer spectra of $Fe_{0.8}Co_{2.2}O_4$ nanocages before and after reaction. The spectra were fitted with two quadrupole doublets. The blue and green doublets were assigned to the octahedral-site (B-site) and tetrahedral-site (A-site) Fe^{III} in $Fe_{0.8}Co_{2.2}O_4$ nanocages, respectively.

The ^{57}Fe Mössbauer spectroscopy is an ideal technique for determining the coordination environment and oxidation state of iron ions in a solid. The Mössbauer spectra of $Fe_{0.8}Co_{2.2}O_4$ nanocages before and after reaction were measured to clarify the role of iron ion in activation of PMS (**Fig. 9**). Due to the superparamagnetic effect of $Fe_{0.8}Co_{2.2}O_4$ nanocages [40], the spectra were fitted with two quadrupole doublets. According to the isomer shift (IS) and quadruple splitting (QS), the blue and green doublets were assigned to the octahedral (B-site) and tetrahedral (A-site) Fe^{III} in $Fe_{0.8}Co_{2.2}O_4$ nanocages, respectively [41, 42]. Negligible changes could be observed after the reaction. Considering that negligible changes could be observed for the BPA removal efficiency with the Fe content in $Fe_xCo_{3-x}O_4$ increasing, the activity probably did not originate from the iron ions in $Fe_{0.8}Co_{2.2}O_4$ nanocages.

5. "Copolymer-co-morphology" conception for shape-controlled synthesis of prussian blue analogues and as-derived spinel oxides

5.1. Synthesis of PBAs and $Mn_xFe_{1.8-x}Co_{1.2}O_4$ nano-dices with controlled morphology

Our strategy for synthesizing PBA copolymer with different morphology, based on a "copolymer-co-morphology" conception, is depicted in **Fig. 10**. When using Fe or M (M = Mn, Co, Zn) salt as the precursors, Fe-Co and M-Co PBA with different morphology could be obtained by the same synthetic method, which is similar to the previous reports [43-46]. When mixing two kinds of PBAs into a solid solution [47, 48], by simultaneously using Fe and M salt as the precursors, the M_yFe_{1-y}-Co PBA copolymer could be easily obtained. It is of great interest and importance to discover that a specific morphology of the copolymer could also be inherited from such strategy. More fascinating phenomenon is that, the final morphology of the PBA copolymer seems to inherit both the shape features of two parent PBAs.

5.2. Cation distribution of the as-prepared $Mn_xFe_{1.8-x}Co_{1.2}O_4$ nano-dices

The cation distribution of the as-prepared $Mn_xFe_{1.8-x}Co_{1.2}O_4$ nano-dices was determined by ^{57}Fe Mössbauer technique in combination with XPS. The 77 K ^{57}Fe Mössbauer spectra of $Mn_xFe_{1.8-x}Co_{1.2}O_4$ nano-dices are shown in **Fig. 11A**. The spectra were fitted with thirteen sextets which follow approximately the binomial distribution of the iron and non-iron cations [49-52]. The isomer shift (IS) range (0.32-0.53 mm s^{-1}) suggests the presence of Fe^{III} ions in high-spin valence state in these spinel oxides. There is a definite difference between the IS values for A-site and B-site Fe^{III} ions. The bond separation Fe-O is larger for B-sites as compared to that for A-sites and thus a larger isomer shift at B-sites is expected [49-52]. According to this, the obtained seven sextets (green) were assigned to A-site Fe^{III} and the other six (orange) were assigned to B-site Fe^{III}. Therefore, a definite ratio of Fe^{III} at A and B-site of the spinel oxides

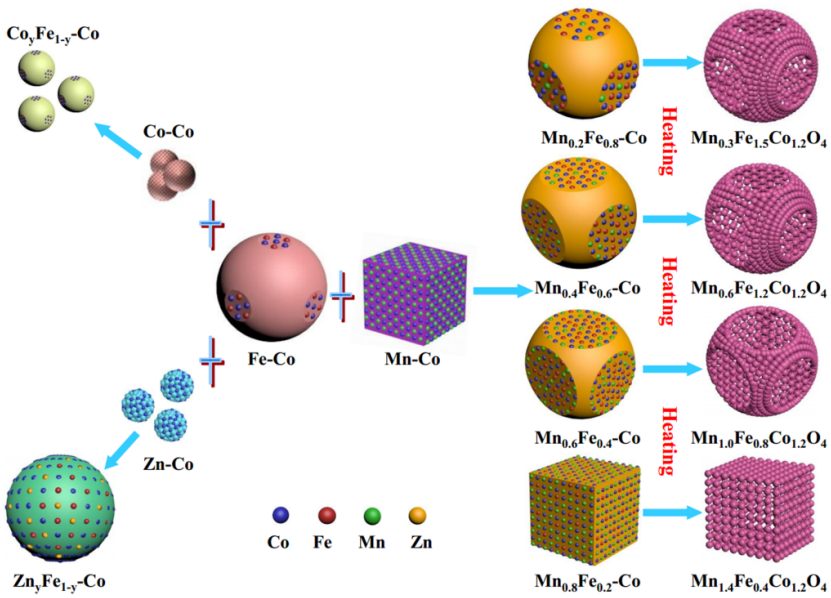

Fig. 10. chematic illustration of the "copolymer-co-morphology" conception for shape-controlled synthesis of Prussian blue analogues and as-derived spinel oxides: if polymer "A" (Fe-Co PBA) and "B" (M-Co PBA) with different morphology could be prepared using the same method, the as-prepared copolymer "AB" (M_yFe_{1-y}-Co PBA) would have one certain morphology, which inherited both the shape feature of polymer "A" and "B". The morphologies were drawn according to the SEM or TEM results (Fig S1), the small colorful balls were used to reflect the changing of the composition.

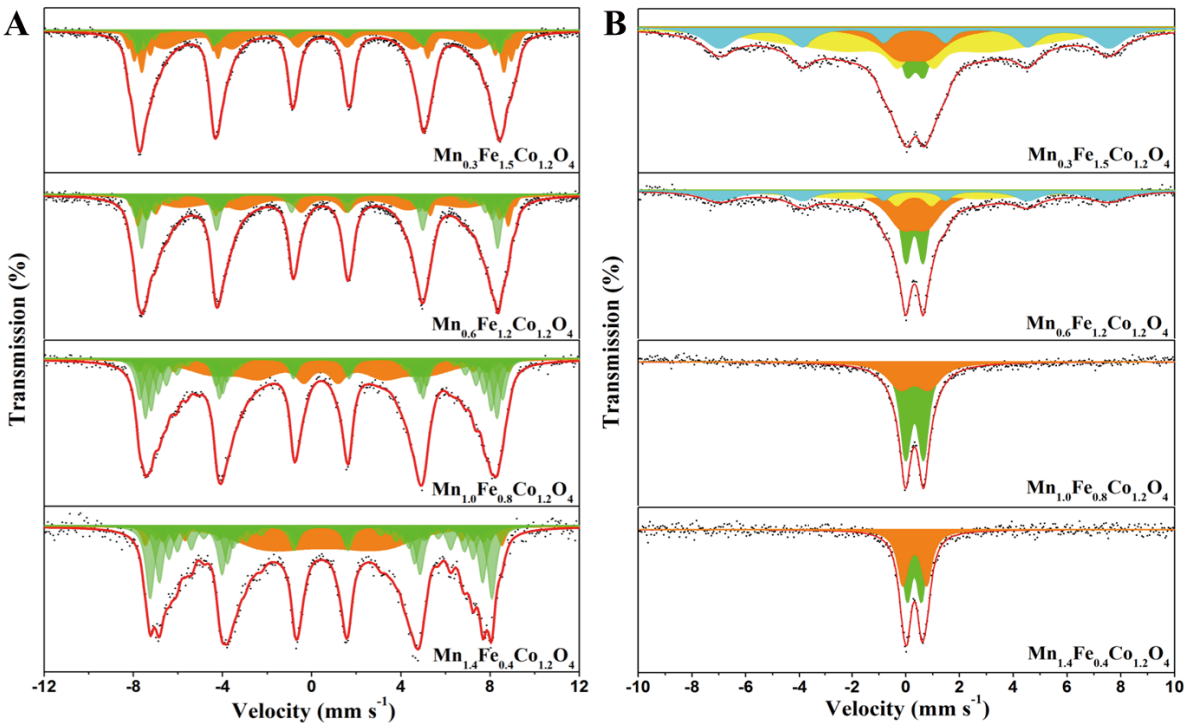

Fig. 11. (A) 77 K ^{57}Fe Mössbauer spectra of $Mn_xFe_{1.8-x}Co_{1.2}O_4$ nano-dices fitted follow the binomial distribution of the iron and non-iron cations. The spectra were fitted with thirteen sextets. In agreement with the fitted IS values, seven sextets (green) were assigned to the tetrahedral-site (A-site) Fe^{III} and the other six (orange) were assigned to the octahedral-site (B-site) Fe^{III}. (B) Room temperature ^{57}Fe Mössbauer spectra of $Mn_xFe_{1.8-x}Co_{1.2}O_4$ nano-dices. The cyan sextet and green doublets were assigned to the tetrahedral-site (A-site) Fe^{III}, the yellow sextet and orange doublets were assigned to the octahedral-site (B-site) Fe^{II}.

was determined and shown in Table S3. Substituting Mn for Fe has the overall effect of decreasing the hyperfine field (H_{hf}) at both the A and B sites, which is because that the Mn–O–Fe superexchange is not as strong as the Fe–O–Fe superexchange. Of the three cations Co, Fe, and Mn, it has been reported that Mn is tend to substitute into B sites and displaces Co onto A sites [49-52]. Therefore, the most possible cation distribution of the $Mn_xFe_{1.8-x}Co_{1.2}O_4$ nano-dices was estimated and concluded in **Table 3.**

The room temperature ^{57}Fe Mössbauer spectra of $Mn_xFe_{1.8-x}Co_{1.2}O_4$ nano-dices are shown in **Fig. 11B**. The spectra were fitted with two sextets or together with two quadrupole doublets. According to the IS and quadruple splitting (QS) [40], the wide and narrow doublet could be assigned to the B-site and A-site Fe^{III} of the spinel oxides, respectively. Similar Fe^{III} ratio at both the A and B-site of the spinel oxides were detected, which is also consistent with the XPS results, further confirming the cation distribution of the as-prepared nano-dices.

Table 3. The chemical compositions, cation distribution, ratios of different cation, surface area, average crystallite size of $Mn_xFe_{1.8-x}Co_{1.2}O_4$ nano-dices

Sample	Cation distribution	Co^{II}/Co^{III}	$Mn^{II}/Mn^{III}/Mn^{IV}$	BET (m^2g^{-1})	Crystallite size (nm)
$Mn_{0.3}Fe_{1.5}Co_{1.2}O_4$	$(Fe_{0.45}Co_{0.55})^A$ $[Fe_{1.04}Mn_{0.31}Co_{0.65}]^B$	71/29	62/22/16	85	9.1
$Mn_{0.6}Fe_{1.2}Co_{1.2}O_4$	$(Fe_{0.56}Co_{0.44})^A$ $[Fe_{0.66}Mn_{0.56}Co_{0.77}]^B$	75/25	37/42/21	86	9.3
$Mn_{1.0}Fe_{0.8}Co_{1.2}O_4$	$(Fe_{0.50}Co_{0.50})^A$ $[Fe_{0.33}Mn_{0.98}Co_{0.70}]^B$	66/34	17/51/32	80	8.6
$Mn_{1.4}Fe_{0.4}Co_{1.2}O_4$	$(Fe_{0.22}Co_{0.78})^A$ $[Fe_{0.18}Mn_{1.39}Co_{0.43}]^B$	66/34	19/50/31	67	8.1

The chemical compositions were analyzed from both EDS and ICP, the cation distribution was obtained from the analysis of Mössbauer spectra, the ratios of different cations were obtained analyzed by XPS, and the average crystallite size was calculated using the Scherrer equation.

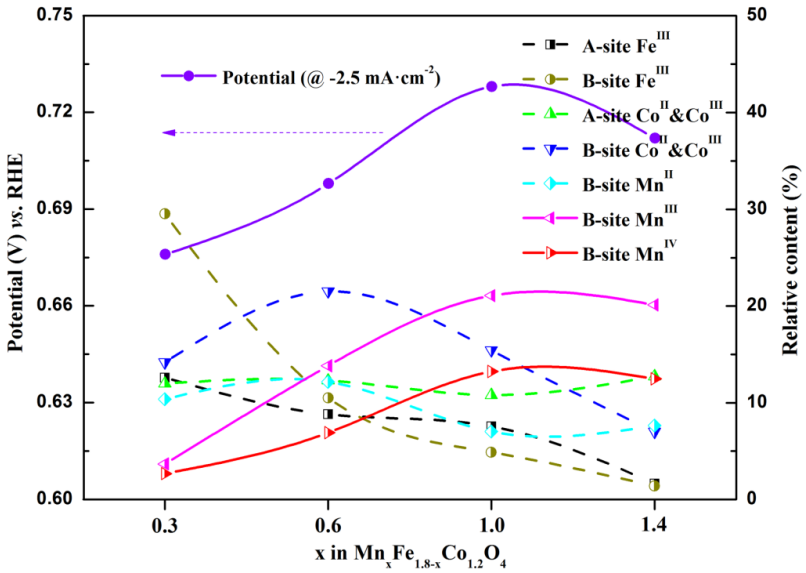

Fig. 12. Structure-function correlations between the ORR activities and the relative contents of A-site or B-site M ions of $Mn_xFe_{1.8-x}Co_{1.2}O_4$ nano-dices.

Fig. 12 shows the structure-function correlations between the ORR activities and the relative contents of A-site or B-site M ions of $Mn_xFe_{1.8-x}Co_{1.2}O_4$ nano-dices. As can be seen, the trend of the half-wave potential of the ORR curve and the current density at 1.7 V of the OER curve were very similar to that of B-site Mn^{III}/Mn^{IV} contents of the catalysts. All these results clearly demonstrate that the B-site Mn^{III}/Mn^{IV} content is the main factor for the electro-catalysis ORR/OER activity.

6. Graphene encapsulated Fe_xCo_y nanocages derived from nanoscale metal–organic frameworks as efficient activators for peroxymonosulfate

6.1. Characterization of FexCoy@C nanocages by Mössbauer spectroscopy

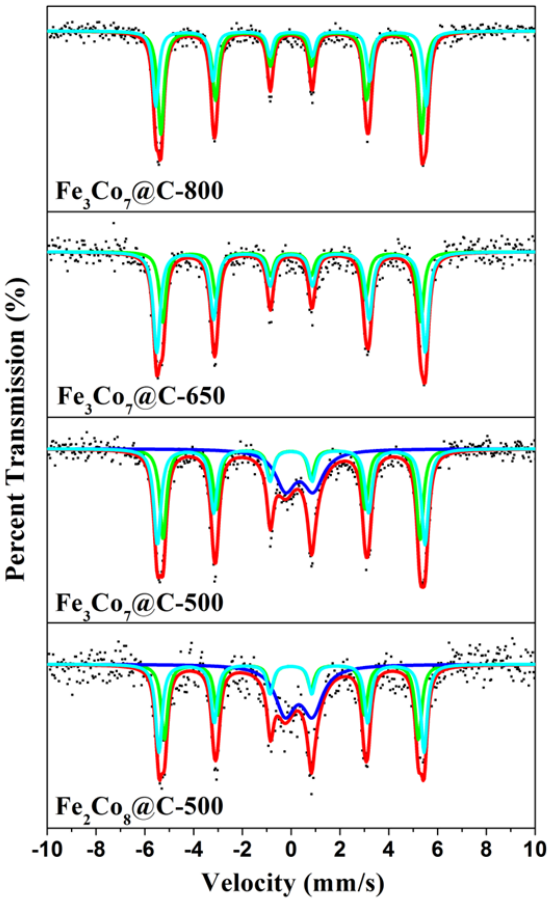

Fig. 13. Room temperature ^{57}Fe Mössbauer spectra of Fe_xCo_y@C nanocages. The spectra were fitted with two sextets, corresponding to two kinds of metallic irons in the Fe_3Co_7 alloy with different chemical environment and/or different crystallite size. The blue doublet in the spectra of Fe_3Co_7@C-500 and Fe_2Co_8@C-500 could be assigned to the Fe^{3+} in Fe_2O_3.

The ^{57}Fe Mössbauer spectroscopy was applied to determining the coordination environment and oxidation state of Fe ions in the samples (**Fig. 13**). The spectra were fitted with two sextets, corresponding to the Fe_3Co_7 alloy in different chemical environments and/or with different crystallite sizes [53]. The blue doublet in the spectra of Fe_3Co_7@C-500 and Fe_2Co_8@C-500 could be assigned to the Fe^{III} in Fe_2O_3. As can be seen, only Fe_3Co_7@C-650, and Fe_3Co_7@C-800 contain the pure phase of Fe metal. The other two samples obtained by heating Fe_yCo_{1-y}-Co PBAs at 500 ºC contain more than 20% percentage of Fe_2O_3, suggesting that heating temperature largely affect the oxidation state of iron ions in the samples.

7. Topotactic transformation of metal–organic frameworks to graphene encapsulated transition metal nitrides as efficient Fenton-like catalysts

7.1. Synthesis and characterization of graphene encapsulated TMNs ($Fe_xMn_{6-x}Co_4$-N@C)

The MOF precursors, Mn_yFe_{1-y}-Co PBAs, were prepared similarly to our previous report [23]. The SEM images of the PBAs reveal the well-controlled morphology of the four samples like nano-dices with good dispersity. A TG-DSC profile of $Mn_{0.4}Fe_{0.6}$-Co PBA under N_2 atmosphere indicates two decomposition stages. The weight loss at the first stage (below 215 ºC) could be ascribed to the loss of water molecules from the MOFs structure. The following weight loss at the second stage (over 455 ºC) could be ascribed to the conversion of MOFs structure to the final products. As illustrated in **Scheme 1**, through thermal decomposition of Mn_yFe_{1-y}-Co PBAs at 650 ºC in N_2, the CN^- group of PBAs will serve as nitrogen and carbon sources to form of nitrogen doped graphene layers [54-56]. Meanwhile, Co and Fe atoms will form FeCo alloy while Mn atoms will form Mn_4N nanocrystals inside, which was most probably due to the same crystal system (Cubic) and space group (Pm-3m) of FeCo and Mn_4N. The final obtained $Fe_xMn_{6-x}Co_4$-N@C particles, constructed from the small FeCo and Mn_4N nanocrystals encapsulated in graphene layers, will inherited the morphology of Mn_yFe_{1-y}-Co PBAs.

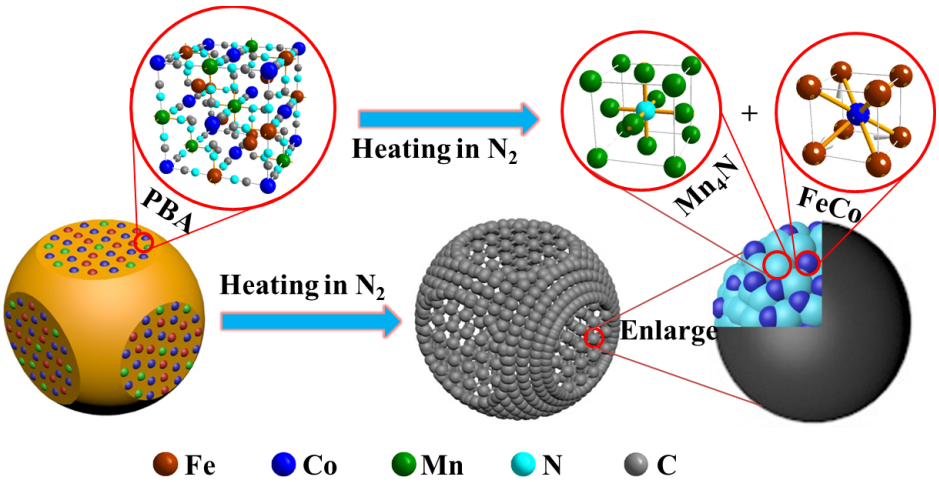

Scheme 1. The preparation route and model of the graphene encapsulated TMNs ($Fe_xMn_{6-x}Co_4$-N@C) with well-controlled morphology

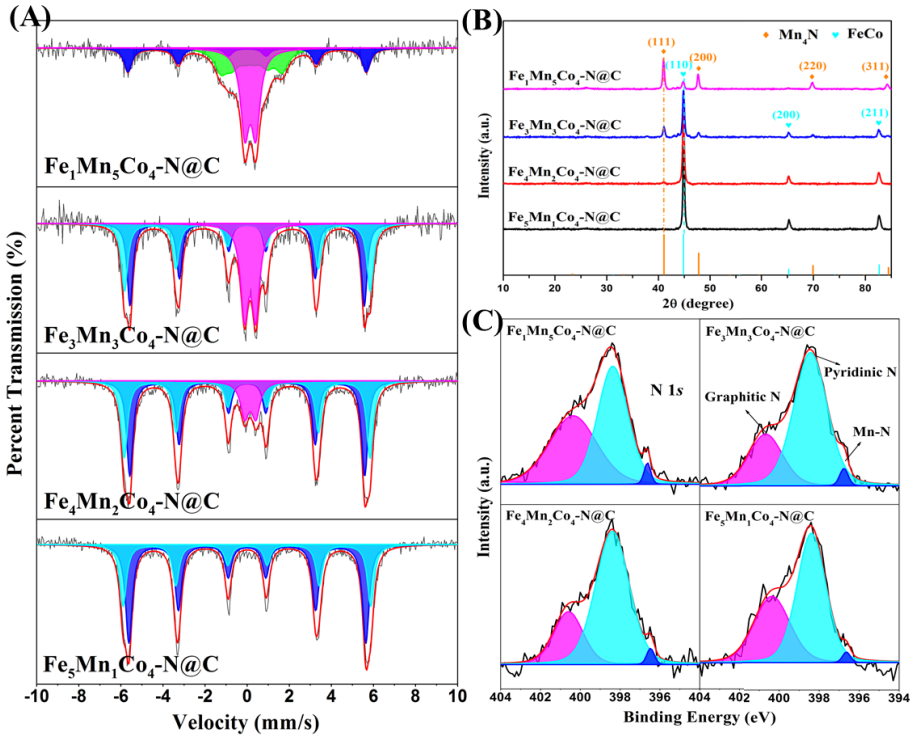

Fig. 14. (A) Room temperature ^{57}Fe Mössbauer spectra of $Fe_xMn_{6-x}Co_4$-N@C nano-dices. The latter three spectra were fitted with two sextets, corresponding to two kinds of metallic irons in the FeCo alloy with different chemical environment and/or different crystallite size. The magenta doublet and the green sextet in the upper three spectra could be assigned Fe_4N. (B) XRD patterns (C) High resolution XPS spectrum of N 1*s* of $Fe_xMn_{6-x}Co_4$-N@C nano-dices.

^{57}Fe Mössbauer spectroscopy was applied to investigate the coordination environment and oxidation state of Fe ions in the samples (**Fig. 14A**). The four spectra were fitted mainly with two sextets, which could be assigned to two kinds of metallic irons in the FeCo alloy with different chemical environment and/or different crystallite size [53]. According to the isomer shift (IS) and hyperfine field (B_{hf}), the magenta doublet and the green sextets in the upper three spectra could be assigned Fe_4N [57]. The B_{hf} value of the green sextet in $Fe_5Mn_1Co_4$-N@C (9.0 T) was found much smaller than the literature reported value (21.6T), which is most probably due to the substitution of the Fe by Mn [58]. In addition, the high resolution XPS spectra of N 1*s* of $Fe_xMn_{6-x}Co_4$-N@C

nano-dices were fitted with three individual peaks, corresponding to nitrogen bound to the metal (Mn-N and Fe-N; 396.6 eV), pyridinic N (398.4 eV), and graphitic N (400.7 eV), respectively (**Fig. 14C**) [59]. All these results suggest that the graphene encapsulated TMNs ($Fe_xMn_{6-x}Co_4$-N@C), with Mn_4N and FeCo alloy as the main phase and well-controlled morphology could be successfully synthesized through the one-step thermal decomposition of Mn_yFe_{1-y}-Co PBAs.

7.2. Activation mechanism of PMS over $Fe_xMn_{6-x}Co_4$-N@C

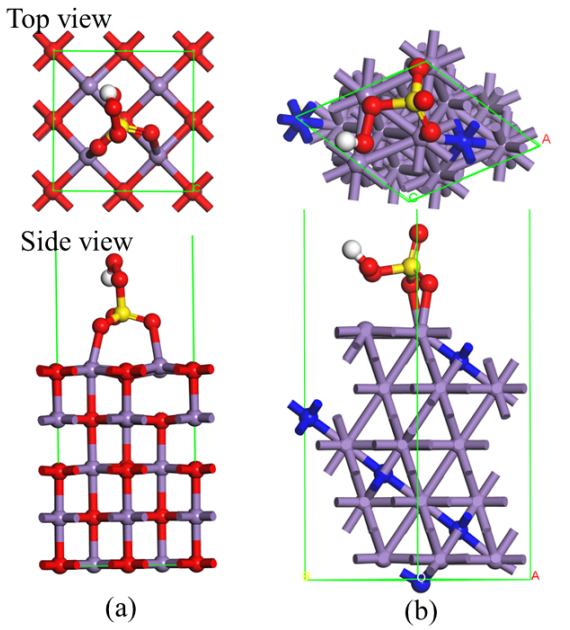

Fig. 15. The atomic configuration of PMS on MnO (200) [panel (a)] and Mn_4N (111) surfaces [panel (b)], respectively. The red, yellow, white, purple, and blue spheres are O, S, H, Mn, and N atoms, respectively

To better understand the effect for PMS activation on MnO and Mn_4N, density functional theory (DFT) calculations are performed to investigate the adsorption of PMS on MnO and Mn_4N surfaces. Based on experimental results, MnO (200) and Mn_4N (111) are chosen in the calculations. After considering all the possible adsorption sites and orientation of PMS, **Fig. 15** shows the relaxed atomic structures of a PMS molecule adsorption on MnO (200) [panel (a)] and Mn_4N (111) surfaces [panel (b)], respectively. For the adsorption on MnO (200) surface, it shows that the PMS is standing on the MnO (200) surface with the two O atoms on $-SO_4$ side bonding with two Mn atoms on surface. The two bond lengths are 2.094, 2.277 Å, respectively. For the adsorption of PMS on the Mn_4N (111) surface, the PMS is laying down with the OH group on the left, and two O atoms from $-SO_4$ group bind with two Mn atoms on the surface. To better understand the interaction between the surfaces and PMS, also for the activation of PMS, The adsorption energy (or binding energy for this case) E_{ads} can be determined by $E_{ads} = E_{tot} - E_{MnO} - E_{PMS}$, where E_{tot}, E_{MnO}, and E_{PMS} are the energies of the MnO surface with PMS adsorption, the MnO surface, and the PMS molecule, respectively. The adsorption on both surface is quite strong with E_{ads} being -4.0 and -5.23 eV for MnO (200) and Mn_4N (111) surfaces, respectively. This also agrees with the formation of covalent bonds between PMS and the two surfaces as shown in **Fig. 15**. Comparing the two surfaces, the adsorption of PMS on Mn_4N (111) is stronger with stronger E_{ads}, longer l_{O-O}, and more electrons received on PMS. Therefore, the PMS on the Mn_4N (111) is more active.

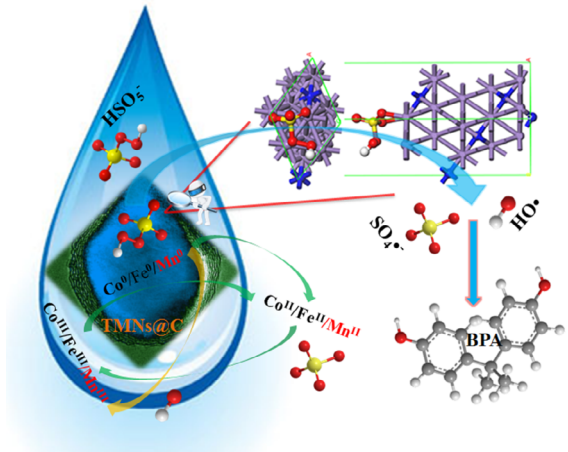

Fig. 16. The proposed mechanism for PMS activation over $Fe_xMn_{6-x}Co_4$-N@C nano-dices.

To investigate the activation mechanism, the involved radicals produced during the PMS activation were investigated using radical scavenger experiments. High resolution XPS spectra of the used catalyst were applied to further explore the PMS activation mechanism. The overall mechanism of PMS activation over $Fe_xMn_{6-x}Co_4$-N@C nano-dices could be proposed as following (**Fig. 16**). Firstly, $\equiv Co^0/Fe^0/Mn^0$ in $Fe_xMn_{6-x}Co_4$-N@C could activate PMS to produce $SO_4^{\bullet-}$ and •OH radicals through **Eqs. 17, 18** with itself oxidized to $\equiv Co^{2+}/Fe^{2+}/Mn^{2+}$ and $\equiv Co^{3+}/Fe^{3+}/Mn^{3+}$,

respectively [59, 60]. Secondly, the generated $\equiv Co^{2+}/Fe^{2+}/Mn^{2+}$ could be quickly oxidized by PMS and produced $SO_4\bullet^-$ radicals (**Eq. 19**). Both PMS and $\equiv Co^0/Fe^0/Mn^0$ could further reduce $\equiv Co^{3+}/Fe^{3+}/Mn^{3+}$ to $\equiv Co^{2+}/Fe^{2+}/Mn^{2+}$ and thus makes the reaction proceed cyclically until PMS was completely consumed [61-63]. In addition, the stronger E_{ads}, longer $l_{O\text{-}O}$, and more electrons received on PMS catalyzed by Mn_4N, largely enhanced the catalytic activity of $Fe_xMn_{6-x}Co_4$-N@C.

$$Co^0/Fe^0/Mn^0 + 2HSO_5^- \rightarrow Co^{2+}/Fe^{2+}/Mn^{2+} + 2SO_4\bullet^- + 2OH^- \quad (17)$$

$$Co^0/Fe^0/Mn^0 + 3HSO_5^- \rightarrow Co^{3+}/Fe^{3+}/Mn^{3+} + 3SO_4^{2-} + 3\bullet OH \quad (18)$$

$$Co^{2+}/Fe^{2+}/Mn^{2+} + HSO_5^- \rightarrow Co^{3+}/Fe^{3+}/Mn^{3+} + SO_4\bullet^- + OH^- \quad (19)$$

$$Co^{3+}/Fe^{3+}/Mn^{3+} + HSO_5^- \rightarrow Co^{2+}/Fe^{2+}/Mn^{2+} + SO_5\bullet^- + H^+ \quad (20)$$

$$Co^0/Fe^0/Mn^0 + 2Co^{3+}/Fe^{3+}/Mn^{3+} \rightarrow 3Co^{2+}/Fe^{2+}/Mn^{2+} \quad (21)$$

$$\bullet OH/SO_4\bullet^- + BPA \rightarrow \text{intermediates} \rightarrow CO_2 \quad (22)$$

Conclusions

This review covers the application of Prussian blue analogues (PBAs) in the research fields such as shape-controlled synthesis of multi-metal nitrides (oxides), and their applications in catalytic activation H_2O_2/PMS based Fenton-like reactions for the removal of organic pollutants. Mössbauer technique results provided strong evidence to investigate the mechanism of the Fenton-like reaction, as well as the relationship between the structure and activity of the catalysts.

Acknowledgements

We gratefully acknowledge financial support provided by the National Natural Science Foundation of China (11079036, 21476232) and the Chinese Academy of Sciences Visiting Professorships for Senior International Scientists (2011T1G15, 2013T2G0009). This work was also partly supported by the China-Egypt Scientific Exchange Project of National Natural Science Foundation of China and Academy of Scientific Research and Technology of Egypt (21311140474) as well as by the European Research Council via contract ERC-StG-259709 and the 'Lendület' (Momentum) Program of the Hungarian Academy of Sciences. X.N. Li thanks Prof. Virender K. Sharma of Texas A&M University, Prof. Hongqi Sun of Edith Cowan University, Prof. Dionysios D. Dionysiou of University of Cincinnati, Prof. Zhaohui Wang of Donghua University for their kind guidance and discussion. Thanks Prof. Dénes L. Nagy of Hungarian Academy of Sciences for helping design the Mössbauer experiments and data analysis. Thanks Prof. Hongxian Han and Prof. Luhua Jiang of Dalian Institute of Chemical Physics for the EPR analysis and the design of electrochemical experiments. X.N. Li is also deeply grateful to his wife Ya Ma for the long-term love and encouragement, best wishes for their lovely baby Zehao Li born recently.

References

[1] M. Munoz, Z.M. de Pedro, J.A. Casas, J.J. Rodriguez, *Appl. Catal. B* **176** (2015) 249-265.

[2] A.D. Bokare, W. Choi, *J. Hazard. Mater.* **275** (2014) 121-135.

[3] P.V. Nidheesh, R. Gandhimathi, S.T. Ramesh, *Environ Sci Pollut Res Int.* **20** (2013) 2099-2132.

[4] E. Neyens, J. Baeyens, *J. Hazard. Mater.* **98** (2003) 33-50.

[5] X. Li, J. Wang, A.I. Rykov, V.K. Sharma, H. Wei, C. Jin, X. Liu, M. Li, S. Yu, C. Sun, D.D. Dionysiou, *Catal. Sci. Technol.* **5** (2015) 504-514.

[6] T. Zhou, X. Wu, J. Mao, Y. Zhang, T.-T. Lim, *Appl. Catal. B* **160** (2014) 325-334.

[7] Y. Qin, F. Song, Z. Ai, P. Zhang, L. Zhang, *Environ. Sci. Technol.* **49** (2015) 7948-7956.

[8] L. Chen, J. Ma, X. Li, J. Zhang, J. Fang, Y. Guan, P. Xie, *Environ. Sci. Technol.* **45** (2011) 3925-3930.

[9] Z. Wang, Y. Guo, Z. Liu, X. Feng, Y. Chen, T. Tao, *Photoch. Photobio. Sci.* **14** (2015) 473-480.

[10] S. Fukuchi, R. Nishimoto, M. Fukushima, Q. Zhu, *Appl. Catal. B* **147** (2014) 411-419.

[11] J. He, X. Yang, B. Men, L. Yu, D. Wang,

J. Mol. Catal. A: Chem. **408** (2015) 179-188.

[12] X. Xue, K. Hanna, C. Despas, F. Wu, N. Deng, *J. Mol. Catal. A: Chem.* **311** (2009) 29-35.

[13] C.K. Duesteberg, T.D. Waite, *Environ. Sci. Technol.* **41** (2007) 4103-4110.

[14] M.D. Paciolla, S. Kolla, S.A. Jansen, *Adv. Environ. Res.* **7** (2002) 169-178.

[15] L. Zhou, Y. Shao, J. Liu, Z. Ye, H. Zhang, J. Ma, Y. Jia, W. Gao, Y. Li, *ACS Appl. Mater. Interfaces* **6** (2014) 7275-7285.

[16] L. Fu, Z. Zhao, J. Ma, X. Hu, *Catal. Commun.* **65** (2015) 96-101.

[17] N. Wang, L. Zhu, M. Lei, Y. She, M. Cao, H. Tang, *ACS Catal.* **1** (2011) 1193-1202.

[18] R. Matta, K. Hanna, T. Kone, S. Chiron, *Chem. Eng. J.* **144** (2008) 453-458.

[19] X. Xue, K. Hanna, C. Despas, F. Wu, N. Deng, *J. Mol. Catal. A: Chem.* **311** (2009) 29-35.

[20] X. Li, J. Liu, A.I. Rykov, H. Han, C. Jin, X. Liu, J. Wang, *Appl. Catal. B* **179** (2015) 196-205.

[21] X. Li, A.I. Rykov, J. Wang, *Catal. Commun.* **77** (2016) 32-36.

[22] X. Li, Z. Wang, B. Zhang, A.I. Rykov, M.A. Ahmed, J. Wang, *Appl. Catal. B* **181** (2016) 788-799.

[23] X. Li, L. Yuan, J. Wang, L. Jiang, A.I. Rykov, D.L. Nagy, C. Bogdan, M.A. Ahmed, K. Zhu, G. Sun, W. Yang, *Nanoscale* **8** (2016) 2333-2342.

[24] X. Li, A.I. Rykov, B. Zhang, Y. Zhang, J. Wang, *Catal. Sci. Technol.* **6** (2016) 7486-7494.

[25] X. Li, Z. Ao, J. Liu, H. Sun, A.I. Rykov, J. Wang, *Acs Nano* (2016).

[26] K. Szacilowski, W. Macyk, G. Stochel, *J. Mater. Chem.* **16** (2006) 4603-4611.

[27] L. Samain, F. Grandjean, G.J. Long, P. Martinetto, P. Bordet, D. Strivay, *J. Phys. Chem. C* **117** (2013) 9693-9712.

[28] C.A. Gorski, M.M. Scherer, *Am. Mineral.* **95** (2010) 1017-1026.

[29] P. Gütlich, Bill, Eckhard, Trautwein, Alfred X., *Springer-Verlag* (2011) 1-569.

[30] L. Samain, B. Gilbert, F. Grandjean, G.J. Long, D. Strivay, *J. Anal. At. Spectrom.* **28** (2013) 524-535.

[31] E. Coronado, M.C. Gimenez-Lopez, T. Korzeniak, G. Levchenko, F.M. Romero, A. Segura, V. Garcia-Baonza, J.C. Cezar, F.M.F. de Groot, A. Milner, M. Paz-Pasternak, *J. Am. Chem. Soc.* **130** (2008) 15519-15532.

[32] H.U.G. Andreas Ludi, *Inorg. Chem.* **14** (1973) 1-21.

[33] A.I. Rykov, J. wangjh, T. Zhang, K. Nomura, *Hyperfine Interact.* **218** (2013) 139-143.

[34] R. Makki, O. Steinbock, *J. Am. Chem. Soc.* **134** (2012) 15519-15527.

[35] J.J. Pignatello, E. Oliveros, A. MacKay, *Critical Reviews in Environmental Science and Technology* **36** (2006) 1-84.

[36] E. Graf, J.R. Mahoney, R.G. Bryant, J.W. Eaton, *J. Biol. Chem.* **259** (1984) 3620-3624.

[37] H. Gallard, J. De Laat, B. Legube, *Water Res.* **33** (1999) 2929-2936.

[38] S.-J. Yuan, X.-H. Dai, *Appl. Catal. B* **154** (2014) 252-258.

[39] A.I. Rykov, X. Li, J. Wang, *J. Solid State Chem.* **227** (2015) 35-44.

[40] B. Pandey, F.J. Litterst, E.M. Baggio-Saitovitch, *J. Magn. Magn. Mater.* **385** (2015) 412-417.

[41] D. Vanidha, A. Arunkumar, S.N. Achary, S. Rajagopan, R. Kannan, *J. Mol. Struct.* **1076** (2014) 105-114.

[42] K. Krieble, T. Schaeffer, J.A. Paulsen, A.P. Ring, C.C.H. Lo, J.E. Snyder, *J. Appl. Phys.* **97** (2005) 107101-107101-107103.

[43] L. Hu, Y. Huang, Q. Chen, *J. Alloys Compd.* **559** (2013) 57-63.

[44] L. Hu, J.-y. Mei, Q.-w. Chen, P. Zhang, *N. Yan, Nanoscale* **3** (2011) 4270-4274.

[45] L. Hu, P. Zhang, Y. Sun, S. Bao, Q. Chen, *Chemphyschem* **14** (2013) 3953-3959.

[46] N. Yan, L. Hu, Y. Li, Y. Wang, H. Zhong, X. Hu, X. Kong, Q. Chen, *J. Phys. Chem. C* **116** (2012) 7227-7235.

[47] Y. Mizuno, M. Okubo, E. Hosono, T. Kudo, K. Oh-ishi, A. Okazawa, N. Kojima, R. Kurono, S.-i. Nishimura, A. Yamada, *J. Mater. Chem. A* **1** (2013) 13055-13059.

[48] D.M. Pajerowski, T. Yamamoto, Y. Einaga, *Inorg. Chem.* **51** (2012) 3648-3655.

[49] D.P. Shoemaker, J. Li, R. Seshadri, *J. Am. Chem. Soc.* **131** (2009) 11450-11457.

[50] T. Franken, R. Palkovits, *Appl. Catal. B* **176–177** (2015) 298-305.

[51]C. Singh, A. Goyal, S. Singhal, *Nanoscale* **6** (2014) 7959-7970.

[52] F. Cheng, J. Shen, B. Peng, Y. Pan, Z. Tao, J. Chen, *Nature Chem.* **3** (2011) 79-84.

[53] T.P. Braga, D.F. Dias, M.F. de Sousa, J.M. Soares, J.M. Sasaki, *J. Alloys Compd.* **622** (2015) 408-417.

[54] M. Zeng, Y. Liu, F. Zhao, K. Nie, N. Han, X. Wang, W. Huang, X. Song, J. Zhong, Y. Li, *Adv. Funct. Mater.* **26** (2016) 4397-4404.

[55] Y. Yang, Z. Lun, G. Xia, F. Zheng, M. He, Q. Chen, *Energy Environ. Sci.* **8** (2015) 3563-3571.

[56] B.K. Barman, K.K. Nanda, *Green Chem.* **18** (2016) 427-432.

[57] U.I. Kramm, I. Herrmann-Geppert, P. Bogdanoff, S. Fiechter, *J. Phys. Chem. C* **115** (2011) 23417-23427.

[58] R.N. Panda, N.S. Gajbhiye, *J. Magn. Magn. Mater.* **195** (1999) 396-405.

[59]Y. Yao, H. Chen, J. Qin, G. Wu, C. Lian,

J. Zhang, S. Wang, *Water Res.* **101** (2016) 281-291.

[60] W.-D. Oh, Z. Dong, T.-T. Lim, *Appl. Catal. B* **194** (2016) 169-201.

[61]C. Cai, H. Zhang, X. Zhong, L. Hou, *J. Hazard. Mater.* **283** (2015) 70-79.

[62]Y. Yao, C. Xu, J. Qin, F. Wei, M. Rao, S. Wang, *Ind. Eng. Chem. Res.* **52** (2013) 17341-17350.

[63]D. He, J. Ma, R.N. Collins, T.D. Waite, *Environ. Sci. Technol.* **50** (2016) 3820-3828.